FeNb and FeSi thermal spraying coatings: microstructure and first principle calculations

N.E. Fenineche*, M. Cherigui, H.I. Feraoun, H. Aourag, C. Coddet

LERMPS, UTBM, 90010 Belfort Cedex, France

Abstract

The development of amorphous and nanocrystalline materials has attracted significant interest in the field of new materials design. Indeed, the magnetic, chemical and mechanical properties of materials are largely enhanced when the size of crystallites becomes nanometric. In addition, the absence of crystal structure implicates a macroscopic behavior fairly different from that of corresponding to the polycrystalline state, especially, mechanical and magnetic properties.

In this work, HVOF and APS thermal spraying were used to produce silicon–iron and niobium–iron alloys coatings. Adjusting the spraying conditions, amorphous coatings were obtained from the FeNb powder. However, for the silicon–iron powder, crystalline deposits were produced in all cases. Boron additives were used to improve the aptitude of the silicon–iron alloy to form an amorphous phase. In this perspective, first principle calculations were elaborated to investigate the electronic structure of crystalline FeNb and Fe_3Si. It was shown that the introduction of boron impurities into the alloy matrix lead to the lowering of the structural stability, and made its electronic density of state (DOS) more comparable to the corresponding niobium–iron structure.
© 2003 Elsevier B.V. All rights reserved.

Keywords: Microstructure; Amorphous coatings; Thermal spraying; Magnetic properties; Iron-based alloys; Rapid quenching; Electronic structures

1. Introduction

Amorphous metallic materials can be obtained by rapid quenching [1] in order to prevent traditional solidification phenomena from occurring. Thus one can obtain materials with disordered structure beyond some interatomic distances. As a consequence, the microstructure does not contain grains as in polycrystals, and so no grain boundaries, elements that control to a large extent the macroscopic behavior. Accordingly, some amorphous metallic alloys exhibit exceptional mechanical, chemical and magnetic properties due to the lack of long range order in their atomic arrangement [2]. However, industrial applications of these amorphous alloys have been restricted due to the difficulties encountered in the production of bulk quantities and the limitations in thickness caused by rapid quenching methods such as melt spinning [2]. There exist a large number of techniques to produce amorphous alloys other than rapid quenching, namely: vapor condensation on cold substrate, cathode sputtering, irons bombardments, electrolysis, and amorphization methods in solid state [3]. Thermal spraying has become very advantageous method owing to the high deposition rates and low operation costs involved [4–7].

Amorphous silicon–iron coatings were produced using thermal spraying. Subsequent trial tests with different spraying conditions were not successful for this alloy, whereas it has been easy to obtain amorphous niobium–iron coatings. Following several suggestions [1], some additive elements within the silicon–iron matrix can lead to an easier amorphization. Looking into the literature, it was found that Fe-SiB amorphous ribbons have been widely used as a magnetic core material and there are also many reports on their crystallization behavior [8,9]. Consequently, a structural and electronic study of crystalline $Fe_{3-x}SiB_x$ and FeNb alloys were initiated via first principle total energy simulation method. The suppercell approach was used to examine the local effect of boron atoms in the silicon–iron structure, and compare the appropriate properties to those of niobium–iron alloy. In this study, niobium–iron alloy is used as a reference material since its amorphization was relatively easy as well as it was stated elsewhere [10].

* Corresponding author. Tel.: +33-3-84-58-31-16;
fax: +33-3-84-58-32-86.
E-mail address: nour-eddine.fenineche@utbm.fr (N.E. Fenineche).

Table 1
HVOF thermal spraying parameters

Parameters	Tube	Plate
Oxygen flow (1 min^{-1})	420	420
Methane flow (1 min^{-1})	140	140
Carrying N$_2$ (1 min^{-1})	20	20
Feed rate (g min^{-1})	35	35
Spray distance (mm)	300	300
Plate speed (m s^{-1})		∼1

2. Experimental study

2.1. Materials and experiments

High velocity oxy-fuel "HVOF" and APS thermal spraying were used to spray Fe-50 wt.% Nb (+0 to 44 μm) and Fe-6.5 wt.% Si (+0 to 150 μm) particles powders. The copper substrate used is a 70 mm × 25 mm and 0.8 mm thick sheet fixed on a port sample moved at a velocity of 200 rpm. The spraying experimental conditions are given in Table 1. To avoid significant heating during the progress of the process, the substrate was cooled on its backside using compressed air. Several passes (15–25) of the torch were necessary to produce 200–300 μm thick coatings.

For microstructural analysis, scanning electron microscopy (SEM) and X-ray diffraction (XRD) (Cu Kα radiation) were used. Details of experimental results have been presented elsewhere [10].

2.2. Calculation method

Our calculations were carried using the full potential linear augmented plane wave (FPLAPW), a first principle total energy density functional theory (DFT)-based method. We used the scalar relativistic version without spin orbit coupling [11] as embodied in the WIEN2k code [12] which is thought to be from the most accurate implementations of the FPLAPW methods for the computation of the electronic structure of solids within density functional theory. In the FPLAPW method, the crystal unit cell is divided into two parts: atomic spheres centered on the atomic sites and an interstitial region. Inside the atomic spheres, the basis set used to describe electronic states employs atomic like functions, while in the interstitial region plane waves are used. Exchange and correlation effects were treated using the generalized gradient approximation (GGA) as described by Perdew and co-workers [13,14].

3. Results and discussion

Fig. 1 illustrates X-rays diffraction patterns for FeNb alloy. Regarding to the peak intensities and their broadening, we noticed a mixture of amorphous and extremely fine crystalline phase (nanocrystalline). This partially amorphous
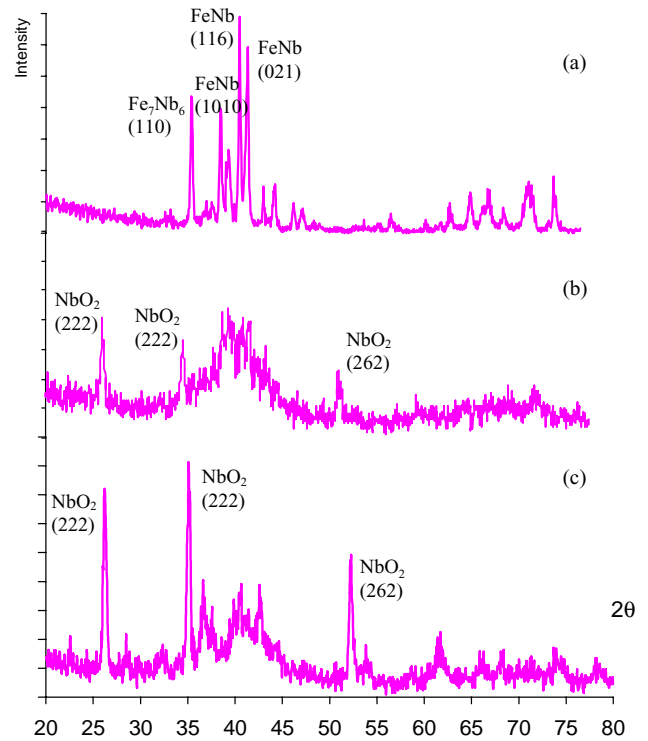

Fig. 1. X-rays diffraction patterns for FeNb (a) powder; (b) HVOF coatings; (c) APS coatings.

structure of FeNb type with the presence of NbO$_2$ and Nb$_2$O$_5$ oxides results from the use of the HVOF technique where the oxidation phenomena are significant. However, for FeSi alloy, the X-rays characterization shows that the structure is perfectly crystalline: the basically cubic structure α1-Fe$_3$Si (DO$_3$), which is characteristic for the low silicon content FeSi alloys is predominant (Fig. 2). These results agree with those obtained by rapidly quenched Fe$_{100-x}$Si$_x$ alloy [15,16] and mechanically alloyed FeSi [17].

Following the X-rays diffraction results, the silicon–iron alloys forms a cubic structure in the *Im3m* (2 2 9) space group, whereas the iron–niobium crystallizes in the rhombohedral *R-3m* (1 6 6) structure. Accordingly, we first undertake the structural optimization of both materials. The total energy was calculated self-consistently for different volumes leading to the energy versus volume plot that we fit to the Murnaghan equation of state [18] to obtain the equilibrium volume, total energy and bulk modulus. In all calculations a set of 200–300 k point where used in the irreducible Brillouin Zone IBZ, and the self-consistent cycles where terminated when both the energy and the charge density reaches an accuracy of 10^{-5}. In the case of FeNb, the c/a ratio was first optimized following the same method, but fitting the energy versus c/a ratio resulting curves to a second order polynomial equation. Fig. 3a and b shows the total energy versus volume change for cubic Fe$_3$Si and rhombohedral FeNb. Table 2 reports the equilibrium calculated lattice parameters, total energies and bulk modulus for both materials.
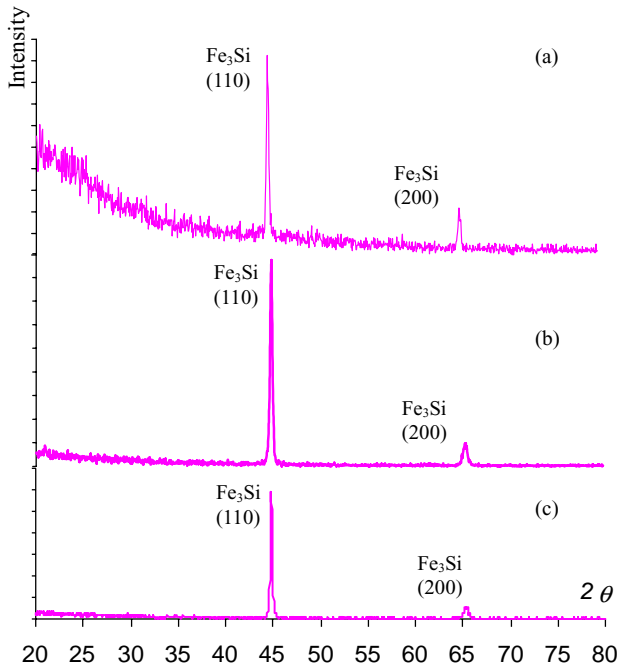
Fig. 2. X-rays diffraction patterns for FeSi (a) powder; (b) HVOF coatings; (c) APS coatings.

Our interest being on the influence of boron impurities in the Fe_3Si lattice on its electronic properties, we have to first find the new lattice parameters after the introduction of boron atoms in the structure. For that we have used the suppercell method: we reduced the symmetry of the lattice by making equivalent positions nonequivalent, we created a translational reproductions of the unit cell, then we removed at each time an iron atom and replaced it by a boron one. Hence, we created doped structures with 8, 16 and 25% of boron. For the Brillouin zone sampling we followed the rule of thumb that stipulates that the size of the k-mesh for the suppercell must be that of the unit cell (original one) multiplied by the ratio of the volumes of simulation cells. This, with the fact that the computational time grow rapidly with growing k-mesh, we were not able to simulate smaller amounts of boron.

As before, we plotted the energy versus volume and fitted to the Murnaghan equation of state. The resultant structural properties are presented in Table 2.

Table 2
Calculated equilibrium volume and bulk modulus for FeNb-, Fe_3Si- and B-doped Fe_3Si compounds

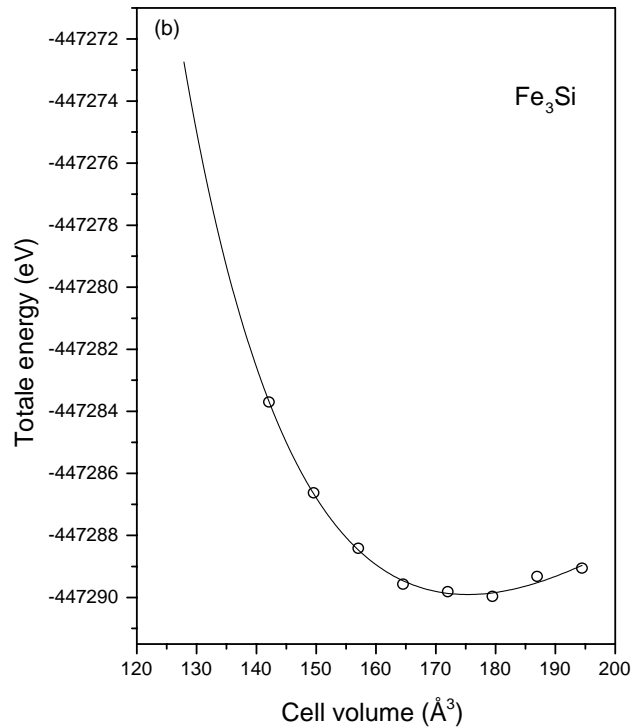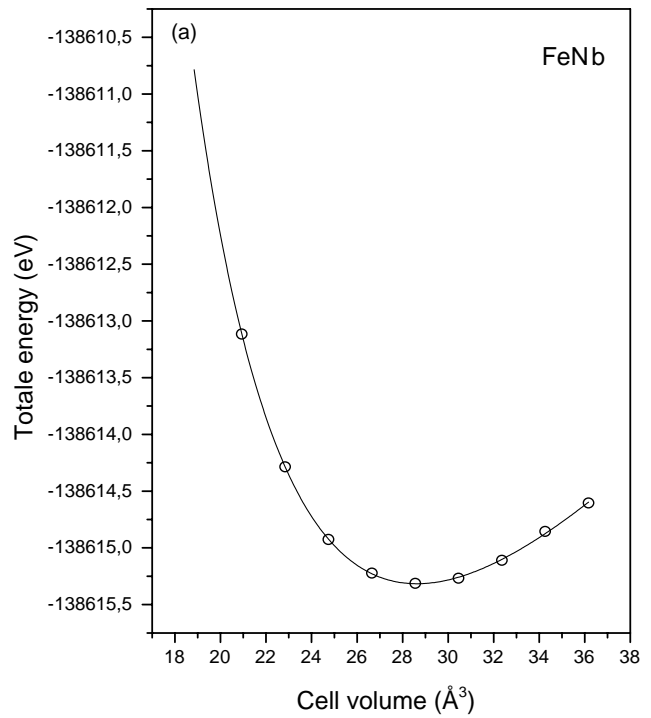|	Equilibrium volume ($Å^3$)	Bulk modulus (GPa)
FeNb	28.63	177.97
Fe_3Si	175.32	183.61
Fe_3Si 8% B	167.42	195.21
Fe_3Si 16% B	160.61	235.40
Fe_3Si 25% B	154.81	252.25

Fig. 3. Total energy vs. volume change for cubic Fe_3Si and rhombohedral FeNb fitted to the Murnaghan equation of state.

Ones the crystal structures optimized, we focus on the electronic properties. We run the self-consistent cycle for each structure, then the electronic density of state (DOS) was calculated using the modified tetrahedron method of Blöchl et al. [19]. Fig. 4 shows the electronic density of state
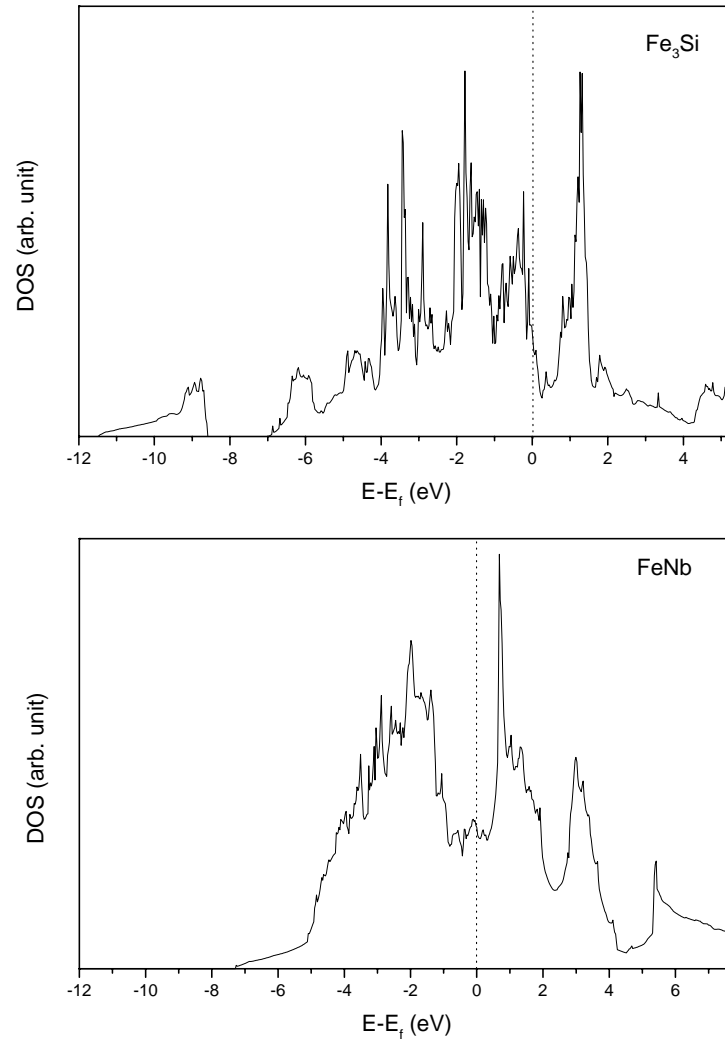
Fig. 4. Electronic density of state of silicon–iron and niobium–iron alloys.

of both alloys. Is represented on the curves, the difference $E - E_{\text{Fermi}}$, so the zero represents the Fermi level. The DOS histograms show the bonding state orbitals near the Fermi level and the top of the density curve with the antibonding states. The major difference that we can assert is the presence in the Fe₃Si histogram of a minimum of density just beyond the Fermi level, separating the peak of the antibonding states, whereas for the FeNb, the Fermi level is directly followed by a pronounced peak. In both compounds, the antibonding states are the localized d states: $4d$ states from iron atoms in both cases, and $3d$ states from niobium atoms in the second. Another difference, is that the peak of the lower energy part of the DOS present for Fe₃Si and which is due mainly to the tightly bounded s states, is not visibly separated from the remaining parts of the DOS for the FeNb alloy. Accordingly, at finite temperatures, the antibonding states are much more populated in the case of FeNb alloy. The minimum of density beyond the Fermi level separating the bonding from the antibonding states in the iron silicon alloy denotes its structural stability.

In Fig. 5, we present the density of state of B-doped Fe₃Si. Fig. 5a–c correspond to 8, 16 and 25%, respectively, of boron in the matrix. We notice that the shape of DOS histogram is different: the addition of boron atoms annihilate gradually the minimum present near the Fermi level. In fact, we see that this minimum is slightly reduced when the boron concentration is of 4%, and is less pronounced for 16% and disappears for 25% of boron. At the same time, we note that the peak present in the bonding state is progressively pronounced, especially, at the Fermi level the density grows with increasing boron concentration. This is in conformity with the calculated values of bulk modulus, which increased with the amount of boron, as shown in Fig. 6.

The fact that the antibonding states are more populated suggests that the addition of boron weaken the crystalline structure stability, even it reinforce the bonds as stated by the increasing bulk modulus. Furthermore, the lowest energy states are progressively connected with the remainder part of the histogram. Both changes make the electronic density of state to be similar to the FeNb one. Therefore,
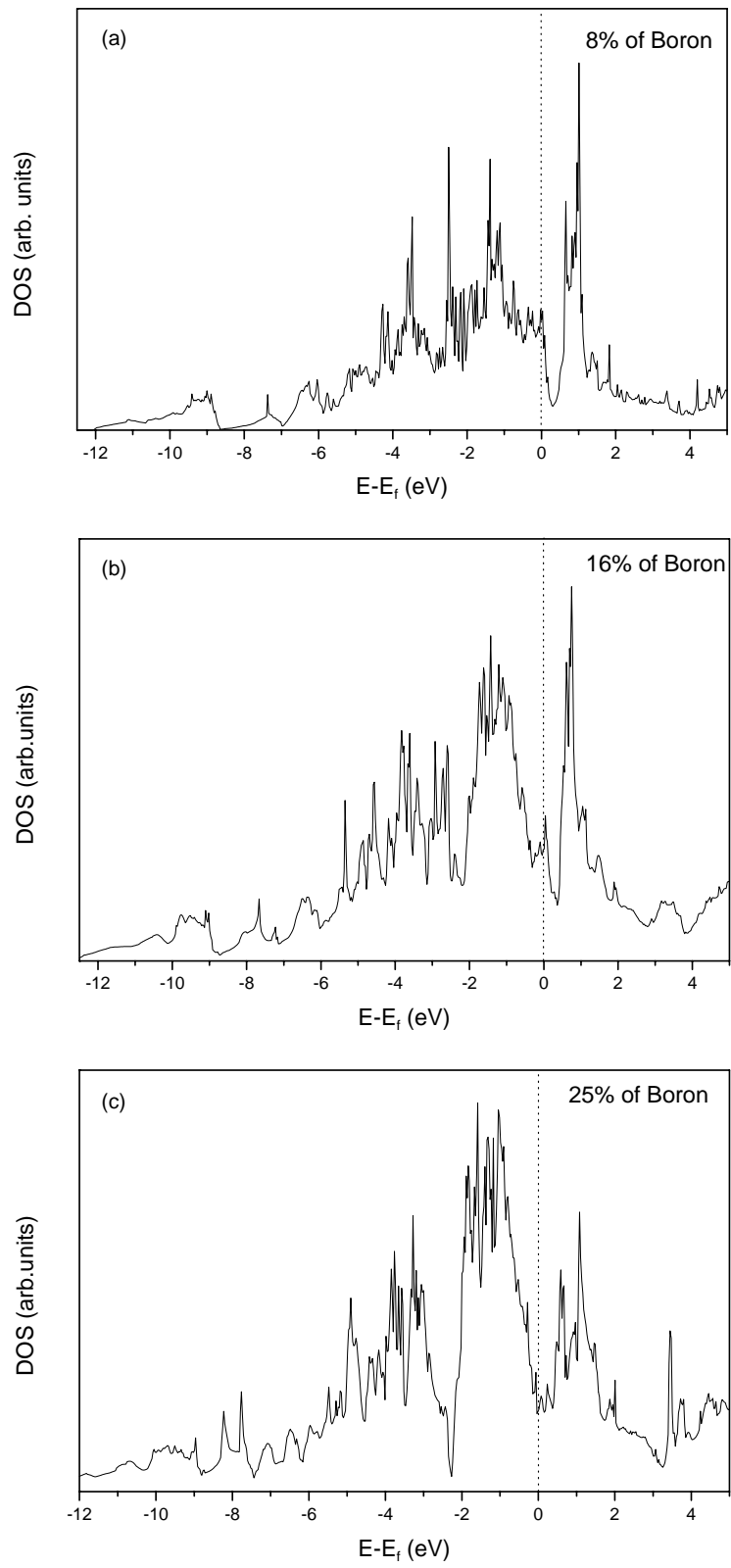
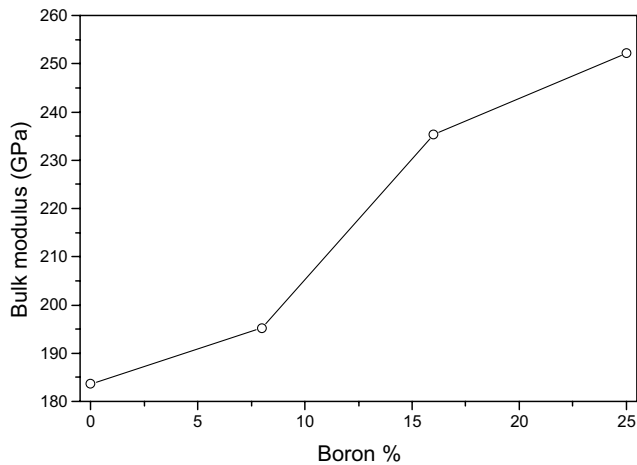Fig. 5. Electronic density of state of boron doped Fe$_3$Si alloy.

Fig. 6. Variation bulk modulus values with Boron content.

the bonding nature in the silicon iron alloy tends to have the same behavior than that of the niobium iron alloy owing to the presence of boron.

4. Conclusion

A combination of experimental and numerical studies on deposits obtained by HVOF and APS thermal spraying of FeSi and FeNb alloys has allowed to compare the FeSiB and FeNb structures. Contrary to the cases of the microcrystalline FeSi deposits, the thermally sprayed FeNb made it possible to obtain coatings with a partially amorphous structure.

Boron atoms were used to improve the aptitude of the silicon–iron alloy to form an amorphous phase. In this perspective, first principle calculations were elaborated to investigate the electronic structure of crystalline FeNb and Fe_3Si. It has been shown that the introduction of boron impurities into the alloy matrix leads to the lowering of the structural stability, and makes its electronic density

of state more comparable to the one corresponding to the niobium–iron structure.

According to the results obtained, and since the crystalline structure stability is intimately bound to the electronic structure properties, the addition of boron in the iron silicon alloy matrix will improve its amorphization ability.

References

[1] J.C. Perron, Constantes Physico-Chimiques, Techniques de l'Ingénieur, vol. K4, 1994.
[2] F.E. Luborsky, Amorphous Metallic Alloys, Butterworths, London, 1983.
[3] R.C. O'Handley, J. Megusar, S.W. Sun, Y. Hara, N.J. Grant, J. Appl. Phys. 57 (1985) 3563.
[4] A. Borisova, Y. Borisov, V. Korzhyk, V. Bobrik, in: Proceedings of ITSC'95, Kobe, May 1995, p. 749.
[5] M. Nakayama, H. Ito, R. Nakamura, M. Toh, A. Ohmori (Eds.), Proceedings of ITSC'95, Kobe, May 1995, p. 1063.
[6] H. Herman, S. Sampath, in: Proceedings of 2nd Plasma Technik Symposium, Lucerne, Switzerland, 1991, p. 63.
[7] G. Föoex, J. Phys. Radium 9 (1938) 37.
[8] T.V. Larionova, O.V. Tolochko, A.S. Zhuravley, Glass Phys. Chem. 21 (1995) 297.
[9] T.V. Larionova, O.V. Tolochko, N.O. Gonchukova, E.V. Novikov, Glass Phys. Chem. 22 (1996) 248.
[10] N.E. Fenineche, M. Cherigui, A. Kellou, H. Aourag, C. Coddet, Proce. Thermal Spray ASA (2003a) 1409–1412.
[11] D.D. Koelling, B.N. Harmon, J. Phys. Solid State Phys. 10 (1977) 3107.
[12] P. Blaha, K. Schwarz, G.K.H. Madsen, D. Kvasnicka, J. Luitz,, WIEN2k, An augmented plane wave + local orbitals program for calculating crystal properties.
[13] J. P Perdew, J.A. Chevary, S. H Vosko, K.A. Jackson, M.R. Pederson, D.J. Singh, C. Fiolhais, Phys. Rev. B46 (1992) 6671.
[14] J.P. Perdew, Y. Wang, Phys. Rev. B45 (1992) 13244.
[15] G.K. Wertheim, V. Jaccarino, J.H. Wernick, J.A. Seitchik, H.J. Williams, R.C. Sherwood, Phys. Lett. 18 (1965) 89.
[16] L.K. Varga, F. Mazaleyrat, J. Kovac, A. Kàkay, Mater. Sci. Eng. A 304–306 (2001) 946–949.
[17] M. Abdellaoui, C. Djega-Mariadassou, E. Gaffet, J. Alloys Compd. 259 (1997) 241–248.
[18] F.D. Murnaghan, Proc. Natl. Acad. Sci. U.S.A. 30 (1944) 244.
[19] P.E. Blöchl, O. Jepsen, O.K. Andersen, Phys. Rev. B49 (1994) 16223.